

See discussions, stats, and author profiles for this publication at: <https://www.researchgate.net/publication/350191330>

# Thermal Performance of Sculptured Tiles for Building Envelopes

Article in *Building and Environment* · March 2021

DOI: 10.1016/j.buildenv.2021.107809

CITATIONS

0

READS

38

5 authors, including:



**Cheli Hershovich**

Technion - Israel Institute of Technology

7 PUBLICATIONS 23 CITATIONS

[SEE PROFILE](#)



**Rene van Hout**

Technion - Israel Institute of Technology

65 PUBLICATIONS 1,162 CITATIONS

[SEE PROFILE](#)



**Vlad Rinsky**

Technion - Israel Institute of Technology

11 PUBLICATIONS 81 CITATIONS

[SEE PROFILE](#)



**Jacob Yasha Grobman**

Technion - Israel Institute of Technology

82 PUBLICATIONS 445 CITATIONS

[SEE PROFILE](#)

Some of the authors of this publication are also working on these related projects:



Fiber reinforced polymers in architectural design and construction [View project](#)



Control of fiber orientation dynamics in the near-field of a coaxial (impinging) jet by flow structure manipulation [View project](#)

# **Thermal Performance of Sculptured Tiles for Building Envelopes**

Cheli Hershcovich<sup>a</sup>, René van Hout<sup>b</sup>, Vladislav Rinsky<sup>c</sup>, Michael Laufer<sup>d</sup> and Yasha j. Grobman<sup>e</sup>

*<sup>a,e</sup> Faculty of Architecture and Town Planning, Technion, Haifa, Israel; <sup>b,c,d</sup> Faculty of Mechanical Engineering, Technion, Haifa, Israel;*

*<sup>a</sup> cheli@technion.ac.il <sup>b</sup> rene@technion.ac.il <sup>c</sup> rinsky@campus.technion.ac.il <sup>d</sup> michael.laufer@campus.technion.ac.il <sup>e</sup> yasha@technion.ac.il*

## Nomenclature

### Roman Symbols

$A_i$	Inner wall surface area [m <sup>2</sup> ]
$A_o$	Outer wall surface area [m <sup>2</sup> ]
$D$	Jet diameter [m]
$d$	Wall layer thickness [cm]
$H$	Distance of jet exit from impingement target [m]
$h_o$	Convective heat transfer coefficient at the outside wall [W/m <sup>2</sup> K]
$I$	Improvement factor $[(q_g^f - q_g)/q_g^f] \times 100\%$
$k$	Thermal conductivity [W/mK]
$q_g$	Global heat transfer rate [W]
$q_g^f$	Global heat transfer rate obtained for a baseline flat tile [W]
$R$	Thermal resistance (R value) [m <sup>2</sup> K/W]
$Re$	Reynolds number (ratio of inertial forces to viscous forces)
$r_i$	Convective heat transfer resistance at the interior wall [m <sup>2</sup> K/W]
$r_o$	Convective heat transfer resistance at the exterior wall [m <sup>2</sup> K/W]
$T_i$	Inner wall temperature [°C]
$T_{\infty,o}$	Free stream temperature [°C]
$U_i$	Overall heat transfer coefficient (U value) $1/R$ [W/m <sup>2</sup> K]
$U_j$	Jet exit velocity [m/s]
$U_r$	Radial velocity component [m/s]
$U_z$	Wall-normal velocity component [m/s]
$\nu$	Kinematic air viscosity [m <sup>2</sup> /s]

### Greek Symbols

$\varepsilon$	Turbulent kinetic energy dissipation [m <sup>2</sup> /s <sup>3</sup> ]
$\rho$	Density [kg/m <sup>3</sup> ]
$\Delta x$	Wall thickness [m]

## **Abstract**

Since effective thermal insulation of buildings could significantly decrease energy consumption worldwide, this study examined the potential of concrete tiles with complex geometries at improving thermal performance in building envelopes. The study focused on air flow characteristics that occur near the external surface of the tile, and their influence on the rate of heat transfer within the material. Six groups of sculptured tiles were developed, using a systematic approach (i.e., repetition of basic geometries), biomimicry, and inspiration from natural envelopes. Air flow behavior and heat transfer rates were examined at three different wind speeds, through both experiments and computational fluid dynamics simulations using a configuration of flow impingement that can be regarded as the worst case scenario. After successfully validating the data, additional numerical simulations were conducted for all developed tiles using the Star-CCM+ commercial software. The results showed an improvement in the insulation performance of about half of all the tested cases. Moreover, significant improvements were seen in the geometries that mimicked animal fur, achieving heat transfer rates that were up to 24% lower than those achieved by smooth tiles. Our results indicate that the application of such tiles with increased thermal resistance could save on thermal insulation materials and improve the thermal performance of building façades.

**Keywords:** microclimate; computational fluid dynamics simulations; computational fluid dynamics experiments; building envelope; thermal insulation

### **1. Introduction**

About 40 percent of the world's energy consumption is accounted for by buildings alone, which could be considerably reduced through proper thermal insulation of the building envelope. Thermal insulation in buildings is traditionally achieved by stacking layers of insulating materials, thereby creating a laminated orthogonal façade. However, effective thermal insulation can also be achieved through additional methods. For example, unique envelope geometries in nature are used by desert

succulents and arctic animals to survive in harsh climatic conditions (Badarnah et al., 2010; Laver et al., 2008). Nature's approach to insulation demonstrates that thermal performance is affected not only by the material itself, but also by the organization of the material in the given space.

Contemporary tools and technologies used by architects have made the design and fabrication of complex geometries achievable. In turn, the availability of these design and fabrication tools has led to an increasing interest in the use of complex geometries in architecture (Grobman, 2008). Moreover, extensive research has been conducted on the aesthetic and practical ramifications of implementing complex geometries in architecture design and fabrication. However, few studies have examined their performance (Grobman, 2010).

Complex geometries in architecture are not new. In the 19<sup>th</sup> century, Antoni Gaudi was one of the first architects to introduce complex geometries into the architectural discourse. He designed and led the construction of organic, highly intricate building elements using a range of techniques that were available at that time, such as stereotomy, and sculptures. In the mid-20<sup>th</sup> century, architects such as Eladio Dieste and Erwin Hauer developed new methods for the realization of complex surfaces that enabled the creation of new architectural languages (Hauer 2004; Stanford 2004). During the 1990s, computer-aided modelling and manufacturing tools emerged, gradually making the design and fabrication of complex geometries readily available to architects and designers. Based on these tools, new architectural styles were developed, such as blob-architecture (Waters, 2003). In an additional process starting in the 1970s, the ability to evaluate the performance of architectural forms developed following the emergence of computational simulations. Rules of thumb and estimations of the geometry's anticipated performance began to be replaced with more accurate calculations (Grobman & Neuman, 2013). Today, the easy access to describing, evaluating, and fabricating almost every form imaginable enables the creation of high-performance and optimized complex geometries.

Studies have demonstrated the impact of geometries on changes to the airflow that in turn improve thermal performance, from micro-level of building façade surfaces to

the macro-level of a city. Large-scale studies showed that air movement within the city depends on morphology, street design, orientation, and form (Golany, 1996). Examining the shape of domed roofs in Persian deserts revealed their ability to create higher air velocities above the vaulted section, thereby enhancing heat transfer and maintaining the thermal comfortability of the interior spaces (Golneshan & Yaghoubi, 1990).

Micro-scale studies have been conducted. For example, Montazeri & Blocken (2013) examined the impact of balcony shapes on airflow and showed that their shapes can strongly impact wind pressure distribution, by creating flow separation, recirculation, and reattachment. Additional studies found that the density and geometry of porosity affect the micro-scale flow patterns near porous screens demonstrating the power of geometry in shaping air patterns (Hrynuik et al., 2012; Latifi Khorasgani et al., 2016). Other studies demonstrated an immediate performative variation, incited purely by surface morphology. Cupkova and Azel (2015) used thermal cameras to scan the back surface of smooth and rough tiles. They showed that rough geometries with larger surface areas had better thermal resistance. Seibold et al. (2018) developed a pavilion of ceramic tiles using an opposite approach, i.e., a contoured, sinusoidal texture designed for optimizing the surface area/thermal mass ratio, thereby maximizing the cooling potential through natural ventilation and buoyancy.

Other researchers employed a biomimetic approach for enhancing the thermal performance in building envelopes. A study by Badarnah et al. (2010) examined various strategies for enhancing thermoregulation based on insights stemming from nature, as well as the shading strategy of leaves based on their organizational features (Badarnah & Knaack, 2008). Laver et al., (2008) suggested a cellular structure for a high-performing masonry wall system based on insight from termites and barrel cacti. Finally, Fechey-Lippens and Bhiwapurkar (2017) developed a biomimetic building envelope that lowers energy consumption while minimizing energy needs for thermoregulation, inspired by the adaptive strategies of the African reed frog and the Hercules beetle.

Based on these studies, we hypothesized that changing the geometry of a flat smooth façade tile can shape air patterns on the surface. In turn, these patterns could then potentially thicken the boundary layer, resulting in improved insulation of the surfaces.

The goal of this paper is to develop a methodology for creating new energy-efficient types of building enclosures and for evaluating their thermal performance. We chose to use concrete tiles in the study as they have been found to encompass the potential of basic shape cavities that improve thermal resistance (Grobman, 2013; Grobman & Elimelech, 2015). The following section presents the methodology that we developed for examining the heat transfer characteristics of various types of façade concrete tile geometries.

## **2. Methodology**

As depicted in Fig. 1, four stages were employed in our research methodology: design and development of geometric tiles, preliminary examination of the developed tiles, computational simulations for the geometries, and re-examination of the best performing geometries. In the first stage, five groups of tiles were developed (fur, cavities, bumps, cacti, and sponges) using three different approaches (the systematic approach, biomimicry, and inspiration from nature). Next, we examined the tiles using computational fluid dynamics (CFD) simulations and experiments for validation purposes. This stage enabled us to ensure that the simulations, which necessarily incorporate certain model assumptions, correctly predict the flow behavior associated with the convective heat transfer problem that this study addressed. Following validation, the third stage used the computational platform as the means through which numerous geometries can be examined within a relatively short time while ensuring reliability. Finally, the best performing geometries were re-examined and improved, based on the collected data.

The systematic approach was utilized to define a baseline of the basic shapes. Four shapes of cavities were used on different tiles, yet each individual tile only had one type of cavity (shapes were not mixed on one tile). Two series of tiles were made. For the first series, the cavities were evenly arrayed on each square tile. The four shapes

of cavities were comprised of both round and rectangular parts: rectangle, triangle, circle and trapezoid. In the second series of tiles, the same shapes were used, but this time implemented as bumps protruding from the flat surface rather than cavities. In both series, the basic dimensions, diameter, and depth of the shapes on each tile were identical.

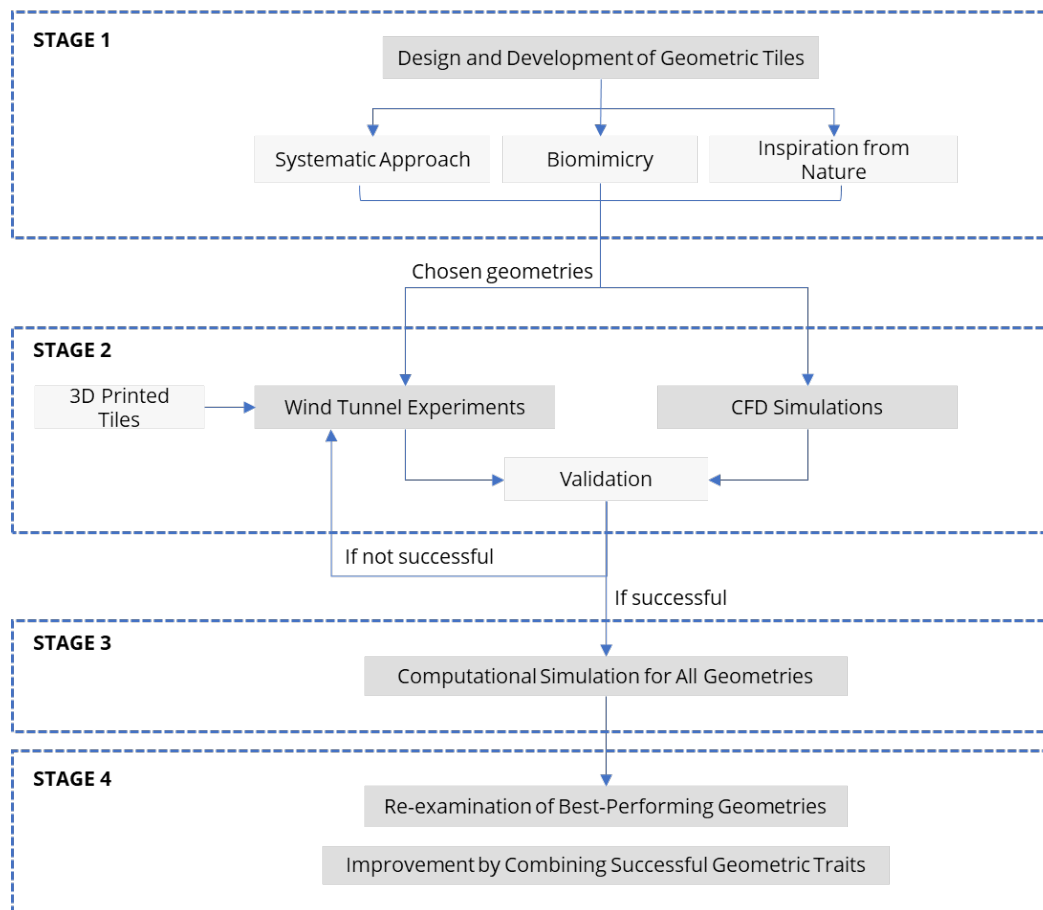


**Fig. 1** The methodology sequence.

The biomimicry and inspiration from nature approaches were based on envelopes naturally found in the environment. These have been optimized through evolutionary processes, resulting in the efficient protection of the inner space of a living organism from external environmental “pressures”. Using biomimicry, natural envelopes of selected succulents (*Oreocereus*, *Ferocactus*, and *Mammillaria compacta*) that live in

harsh arid climatic conditions were reproduced as accurately as possible. The chosen succulents were scanned using a three-dimensional (3D) EVA scanner (ARTEC), with a 0.1mm accuracy. The generated point clouds were imported as meshes onto the Rhinoceros modelling software. As seen in Fig. 2, the repetitive tile geometries were created based on actual cacti textures (Hershovich et al., 2017).

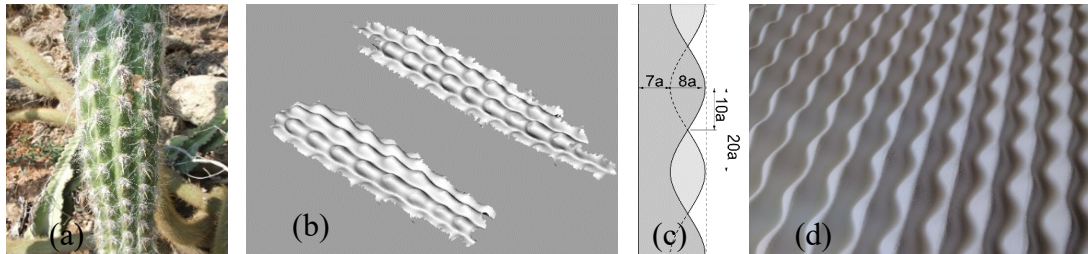


**Fig. 2.** Example of examined cactus.

(a) Oreocereus Cactus; (b) 3D model of the Cactus created by 3D scan; (c) Tile section in line with exact scan proportions; and (d) 3D printed gypsum model that represents the proportions of the cactus.

The third approach, inspired by nature, included groups of animal fur and sponges, and differed from biomimicry in that only one main principle of the natural envelope was mimicked. To create repetitive, comparable tiles, geometric abstraction was used, thereby mimicking the density and basic shapes of animal fur and sponges. A summary of the tiles developed for this study, using all three approaches, are presented in Fig. 3. Moreover, Table 1 adds to this information, presenting data and simulation results regarding the geometrical properties of the tiles, as well as the global heat transfer rates for a range of wind velocities.

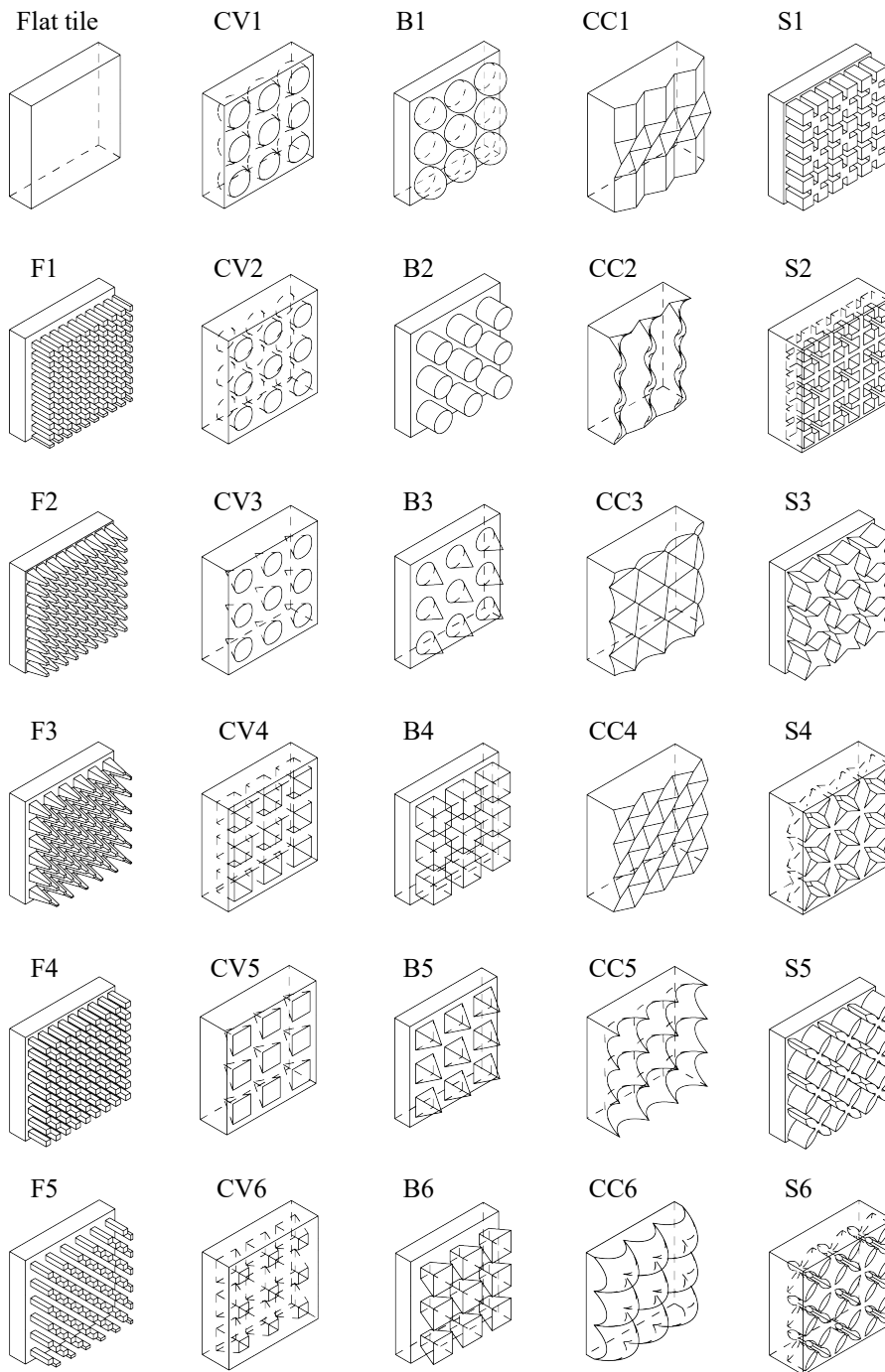


**Fig. 3.** Isometric drawing of the tiles.

From left to right: Column I, flat tile and Fur (F) 1-5; Column II: Cavities (CV) 1-6; Column III: Bumps (B) 1-6; Column IV: Cacti (CC) 1-6; Column V: Sponges (S) 1-6

Tile Type	Volume [mm <sup>3</sup> ]	Exposed Surface Area [mm <sup>2</sup> ]	VR (Volume Ratio)	SAR (Surface Area Ratio)	Global Heat Transfer Rate [W]		
					1 m/s	5 m/s	10 m/s
Flat Tile	600000	40000	1.00	1.00	2.01	4.59	5.83
F1	256832	193664	0.43	4.84	1.74	3.63	5
F2	357976	158649	0.60	3.97	1.77	3.78	5.33
F3	347040	142009	0.58	3.55	1.7	3.62	5.08
F4	344800	169600	0.57	4.24	1.66	3.58	4.98
F5	335712	151424	0.56	3.79	1.62	3.49	4.92
CV1	491729	80398	0.82	2.01	1.95	4.58	6.36
CV2	510103	85238	0.85	2.13	1.99	4.65	6.49
CV3	569840	53979	0.95	1.35	2.04	4.63	6.13
CV4	484800	97600	0.81	2.44	1.96	4.57	6.42
CV5	561600	57797	0.94	1.44	2.04	4.6	6.1
CV6	521133	101159	0.87	2.53	2.01	4.36	5.84
B1	388270	80399	0.65	2.01	2.02	4.94	6.97
B2	370477	85238	0.62	2.13	1.92	4.51	6.06
B3	310159	53979	0.52	1.35	2.08	5.42	7.64
B4	395200	97600	0.66	2.44	2.04	4.91	6.68
B5	318400	57799	0.53	1.44	2.02	4.97	6.79
B6	358866	101161	0.60	2.53	1.8	3.97	5.6
CC1	539973	43264	0.90	1.08	2.07	4.56	6.03
CC2	552334	42473	0.92	1.06	2.07	4.43	5.81
CC3	500000	43535	0.83	1.09	2.06	4.61	6.25
CC4	539973	42582	0.90	1.06	2.08	4.5	5.93
CC5	284824	68326	0.47	1.71	1.7	4.73	6.82
CC6	457794	68326	0.76	1.71	2.1	5.04	6.96
S1	460800	172000	0.77	4.30	2.07	4.49	6.23
S2	419200	172,000	0.70	4.30	2.04	4.48	6.32
S3	405120	129779	0.68	3.24	1.91	4.47	6.42

S4	474880	129779	0.79	3.24	1.94	4.42	6.17
S5	393203	147954	0.66	3.70	1.9	4.34	6.29
S6	486796	147954	0.81	3.70	1.98	4.34	5.97

**Table 1.** Geometric data and simulation results. For graphical representation of the tile types, see Fig. 3.

The ability to fabricate a geometry (i.e., achieve realization) was considered while designing the tiles. The actual overall dimensions (i.e., bounding box) of each designed tile were  $7.5 \times 100 \times 100$  cm<sup>3</sup>. As stated, the chosen tile material was concrete. As the research aimed at examining the influence of the geometric form on heat transfer, the material needed to be basic and simple, and with well-known properties. In addition, since concrete is widely used in buildings, the performance of concrete tiles could be easily compared to typical wall compounds. Moreover, concrete can be easily cast into molds, thereby providing a simple means for creating complex geometries. Finally, concrete is an inexpensive, widely available material that can be used following this study to help maintain climate-protected living among low socio-economic societies.

## 2.1 Experiments

In urban environments, wind is usually turbulent and as a result complex to model and simulate numerically. Moreover, for certain geometric configurations the reliability of existing CFD simulation tools is still questionable and requires experimental validation based on dimensionless similarity. In addition, experiments require vast resources, including funding, time, materials, and equipment maintenance. As a result, experiments are usually only applied to a subset of selected validation cases. In this research, we combined computational tools and experiments. To ensure confidence in the computational tool, we first examined several selected tile geometries in an experiment where an air jet impinged perpendicularly on the tile's surface. This set up represents the worst-case heat transfer scenario inside a building, since at the stagnation point, maximum heat transfer occurs in walls.

Experiments were conducted at the Environmental Multi-Phase Flow Laboratory

(EMPFL) at the Technion-Israel Institute of Technology. An axisymmetric, turbulent air jet was created by installing a converging nozzle (with a contraction area ratio of 100:1) at the end of a small open loop wind tunnel (van Hout et al., 2018a). The exit diameter of the jet was  $D = 20$  mm, and the exit jet velocities were  $U_j = 1, 5$  and  $10$  m/s, corresponding to 1, 3, and 5 on the Beaufort scale. These represented various atmospheric flow conditions, from light air movement to a fresh breeze, that are common in urban and rural environments. Jet Reynolds numbers were  $Re = U_j D / \nu = 1,300, 6,260$  and  $12,354$ , where  $\nu$  denotes the kinematic air viscosity. The surfaces were installed at a distance of  $H = 10$  cm ( $H/D = 5$ ) from the nozzle exit.

Six basic geometry tiles (referred to as CV1-6, Fig. 3) and three cactus tiles (referred to as CC1-3, Fig. 3) were printed using a Z-Crop 350 gypsum 3D printer. To accommodate numerical simulations, tile dimensions were scaled down by a factor of five. As seen in Fig. 4, flow field measurements were performed using a particle image velocimetry (PIV) system (LaVision GmbH), consisting of a charge-coupled device (CCD) camera (2048x2048 pixels), an Nd:Yag laser (200mJ/pulse), laser sheet optics and acquisition/processing software (DaVis 7.4). Using a cylindrical lens, a laser sheet ( $\sim 1$ mm thickness) was created perpendicular to the surface, crossing the jet's center plane. Planar flow field measurements were acquired at 5Hz. At each  $Re$  and tile configuration, 450 instantaneous vector maps were acquired with a field of view (FOV) of about  $100 \times 100$  mm<sup>2</sup>. It should be noted that the tiles were spray painted black, in order to minimize reflections of the laser light from the surface. Moreover, due to the opaqueness of the tested tiles (gypsum), the flow pattern inside the cavities could not be measured. Multi-pass processing (DaVis 7.4, LaVision GmbH) was used to extract the velocity fields that were further processed using in-house developed Matlab codes (MathWorks Inc.).

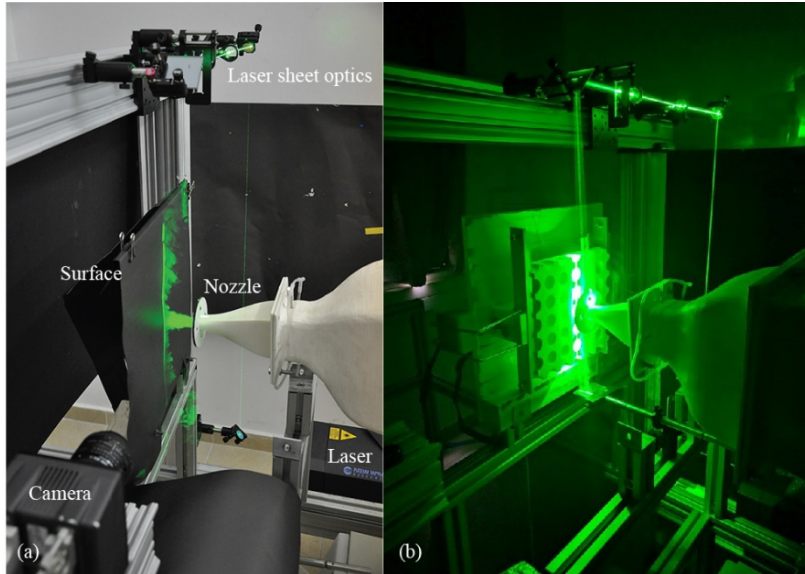


**Fig. 4.** Experimental setup. (a) The experimental setup for the PIV system; (b) Flow visualization on a sculptured surface.

The experimental dataset allowed us to extract ensemble averaged and turbulence characteristics of the flow. For example, Reynolds shear stress distributions that provided information about the turbulent momentum diffusivity, and upon invoking the Reynolds analogy (when appropriate), also on the turbulent heat diffusivity. For a more detailed description of the experimental facility and flow field results, the reader is referred to van Hout et al. 2018a, b and c.

## 2.2 Numerical Simulations

CFD simulations offer considerable advantages compared to wind tunnel experiments, especially in terms of duration and required resources. For this reason, we evaluated the average heat transfer performance of the tiles using CFD simulations. To ensure that these simulations and the experiments were performed under the same conditions, fluid parameters and jet geometry in the CFD simulations and the experiments were matched. The validation of the CFD simulations by the experiments will be discussed in the following (see Section 2.3).

The employed boundary conditions were those of an isothermal and uniform jet

flow at the inlet, and a non-slip, isothermal impingement surface. At the outlet of the computational domain, a constant pressure boundary condition was imposed. Thermal boundary conditions were defined to simulate typical temperature differences seen in a civil structure. The inner wall of the target geometry was maintained at 23°C, while the impinging jet exit temperature and ambient air were kept at 30°C. The side walls of the target surface were defined as adiabatic, thus restricting solid-fluid heat transfer from the bottom to the top surfaces (1D conduction). This formulation takes into account both the conductive heat transfer resistance within the solid, as well as the convective heat transfer resistance at the solid-fluid interface. The less heat that is transferred between the fluid and solid, the higher the thermal resistance or insulation quality. The global heat transfer rate,  $q_g$ , was defined as the amount of heat transferred per unit of time between the solid and fluid region. The steady state value was registered at the point where the simulation was converged, and its value remained constant for a few hundred iterations.

CFD simulations were performed using the commercially available Star-CCM+ 11 CFD package. A 3D simulation was set up for a round jet, with a uniform velocity profile exiting from a 2 cm diameter outlet and impinging perpendicular on the center of the tile. The investigated jet Reynolds numbers matched those of the experiments previously described in Section 2.1. In the simulations, fluid density and dynamic viscosity were taken as constant, and were chosen to match those in the experiments (at a temperature of 28°C). Fluid properties were computed using the Engineering Equation Solver (EES). The numerical simulations were based on the Reynolds Averaged Navier-Stokes (RANS) equations. These were solved using the V2F model (e.g., Behnia et al., 1998) using a slightly modified  $k$ - $\epsilon$  turbulence model and an additional transport equation for the variance of the wall-normal velocity fluctuations. The V2F model was chosen since it offers the most accurate results for impinging jet problems, except for more computationally expensive options, such as Direct Numerical Simulations (DNS) and Large Eddy Simulations (LES) (Zuckerman & Lior, 2005).

Due to the 3D nature of the airflow and the large computational domain, an

optimal mesh was generated. This ensured a reasonable cell count while providing sufficient spatial resolution in areas of particular interest, especially close to the wall. A variable density mesh was generated, whereby smaller cells were used near the target surface and downstream of the jet nozzle, while larger cells were used towards the boundaries of the computational domain, as shown in Fig. 5. This substantially reduced the total number of cells in the grid.

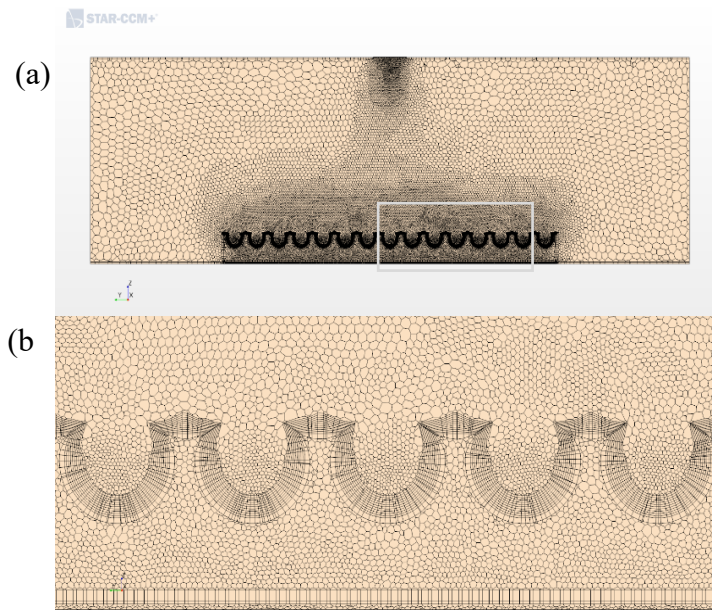


**Fig. 5.** Generated star CCM+ mesh (2D vertical section). (a) Full range; (b) Zoom-in of the area of the white rectangle marked in (a)

### 2.3 Validation between Experiments and Simulations

In order to make sure that the computations faithfully simulate the complex flow field, results of the CFD simulations were compared to several representative and measured ensemble averaged flow fields. An example of such a comparison is provided in Fig. 6 that depicts contour plots of the normalized, ensemble averaged radial velocity fields,  $\langle U_r \rangle / U_j$ , as a function of the normalized radial distance,  $r/D$ , away from the stagnation point and close to the tile ( $z/D = 0$ ). Results are shown for flow over a smooth tile (left-hand column in Fig. 6) and a dimpled tile (right-hand column in Fig. 6). Note that  $\langle U_z \rangle$  is significant mainly in the incoming round jet (not shown), while  $\langle U_r \rangle$  is significant near the wall in the radial direction (Fig. 6). As

observed, the overall flow field is very similar between the simulations and the experiments.

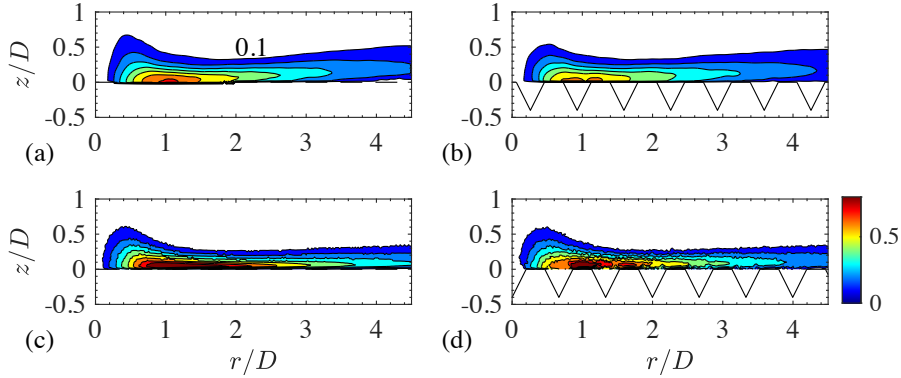


**Fig. 6.** Contour plots of the normalized, mean radial velocity,  $\langle U_r \rangle / U_j$ , away from the stagnation point at  $r/D = 0$  ( $Re = 6,260$ ,  $U_j = 5$  m/s); a comparison between experimental results (top row), and CFD simulations (bottom row). Left-hand column: smooth target surface; right-hand column: dimpled target surface (swept triangle, indicated by saw-tooth pattern in (b) and (d)). Contour levels:  $[0.1:0.1:0.8]$ , with an example contour level value plotted in (a).

Fig. 7 presents a closer look at the mean normalized velocity profiles and comparison between the simulations and experiments. Radial profiles of  $\langle U_z \rangle / U_j$  are plotted close to the jet nozzle exit ( $z/D = 4.5$ , Fig. 7a) and closer to the tile at  $z/D = 2$  (Fig. 7b). Clearly the incoming measured and simulated flow field compare well, although some small asymmetry can be observed in the experimental results. Radial velocity profiles are depicted in Fig. 7c, and d, for the smooth and the dimpled tile. It can be observed that the general profile shapes of the experiments and the simulations are similar. However, the simulated results are more peaked close to the wall and decrease faster away from the wall. This is likely to result in overestimation of the heat transfer (invoking the Reynolds analogy) due to higher near wall gradients. However, the obtained similarity between the shapes of the simulated and the measured velocities provides confidence in the obtained results. Note that similar results were obtained for other selected flow conditions and tiles.

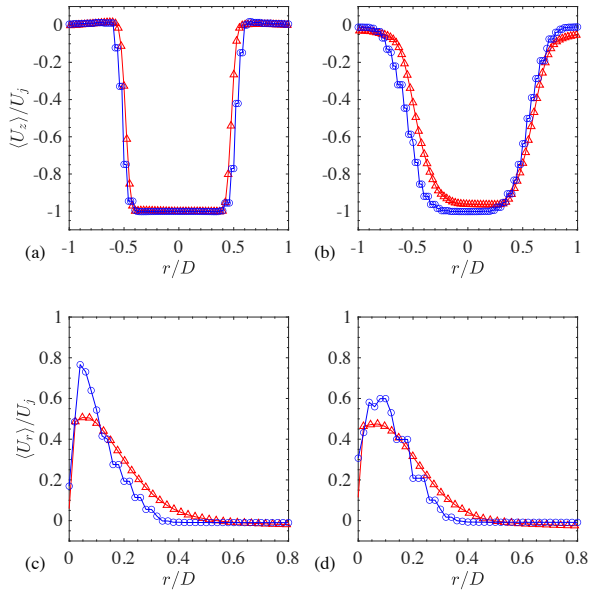


**Fig. 7.** Comparison between the experimental (red triangles) and simulated (blue circles) mean velocity profiles ( $Re = 6,260$ ,  $U_j = 5$  m/s) as a function of  $r/D$ .  $\langle U_z \rangle / U_j$  at  $z/D =$  (a) 4.5, and (b) 2;  $\langle U_r \rangle / U_j$  for (c) smooth, and (d) dimpled surface.

#### 2.4 Radiation Heat Transfer: Geometry Self-Shading

In hot climates, radiation heat transfer is a major contributor to the heat flux on building façades. All of the examined tile geometries increased the exposed surface area compared to flat tiles (as seen in Table 1). This could lead to two opposing effects: either higher solar irradiance gains due to increased exposed surface area, or lower solar irradiance gains due to “self-shading” of the tile’s geometry itself. We therefore explored the possible relationship between the tile geometry and the average annual amount of solar irradiance on its surface. To simulate a tile installed in a full façade and account for the effect of ambient shadows, the tile was divided into nine equal sections. The central unit was monitored, while the other eight units served as context (see Fig. 8a).

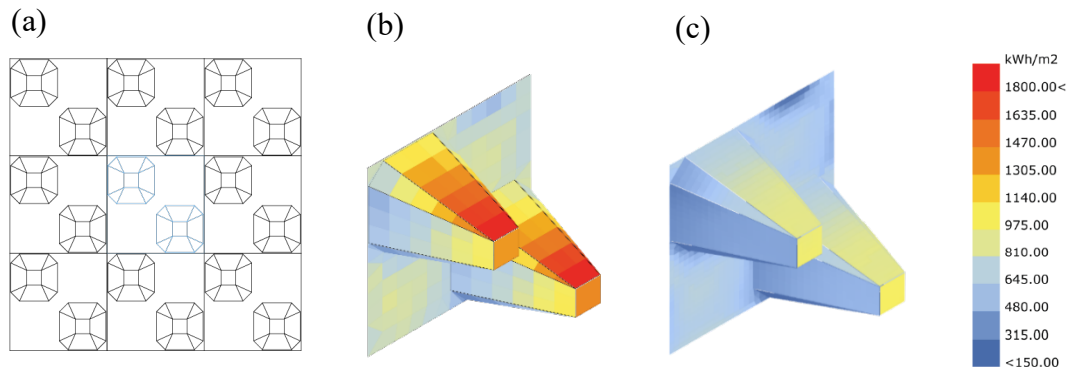


**Fig. 8.** Self-shading of geometric tiles.

(a) Elevation drawing of the divided tile: examined central unit (in blue); (b) Average solar irradiance results of annual simulation; (c) Average solar irradiance results of winter simulation.

Irradiance values were simulated by the scientific-approved tools Ladybug and Honeybee, as part of the Grasshopper plugin for Rhinoceros of McNeel. The simulations were based on climatic data in the standard EnergyPlus weather data file (\*.epw), as measured by the Tel-Aviv Bet Dagan station. An annual simulation was conducted, collecting daily results of accumulative solar irradiance every hour, between 10 am to 2 pm. Monthly averages were calculated based on hourly results. All tiles were vertically positioned, with their external surface facing south. Typical output of the radiation simulation is presented in Fig. 8 (b) and (c). The following chapter presents the results of the study.

### 3. Results

For each test, the CFD simulation provided information regarding the global heat transfer rate (not including radiation), 3D distributions of velocity magnitudes, and the temperature. In the following analysis, we used the global heat transfer rate results from the simulations. Since the bottom of the tile maintains a lower temperature (23°C) than that of the jet nozzle exit flow (30°C), heat is transferred from the jet to the tile. The heat transfer rate is affected by both conduction through the solid

concrete tile and convection between the air and the tile.

Based on values of  $q_g$  for the various investigated tiles, we could identify those that improved thermal performance compared to flat tiles by defining the “improvement factor” as follows:

$$I = [(q_g^f - q_g)/q_g^f] \times 100\%, \quad (1)$$

where  $q_g^f$  denotes the global heat transfer rate obtained for the baseline flat tile. As  $q_g$  decreases, the tile’s thermal resistance (R) increases. Note that R can be interpreted as the temperature difference by which the material resists heat flow [K/W]). Results organized according to ascending global heat transfer rates are summarized in Fig. 9. For ease of comparison, the flat tile results are indicated by a shaded rectangle, so that relative improvement or degradation to the smooth tile can be easily evaluated.

As observed in Fig. 9, at a jet exit velocity of 1 m/s (Fig. 9a), out of the 30 tiles examined, 17 showed improved thermal performance compared to the smooth tiles, with a maximum improvement and degradation of 25% (F6) and 4% (CC6), respectively. At  $U_j = 5$  m/s, the maximum improvement and degradation were 23% (F5) and 18% (B3), respectively, with 20 of the tiles (two-thirds) improving the thermal insulating performance compared to the smooth tiles. Finally, at  $U_j = 10$  m/s, the maximum improvement and degradation were 15% (F5) and 31% (B3), respectively. In this last case, only eight tiles (less than one-third of the tiles) showed improved the thermal insulating performance, and it can be concluded that thermal tile performance varies, depending on the wind speed.

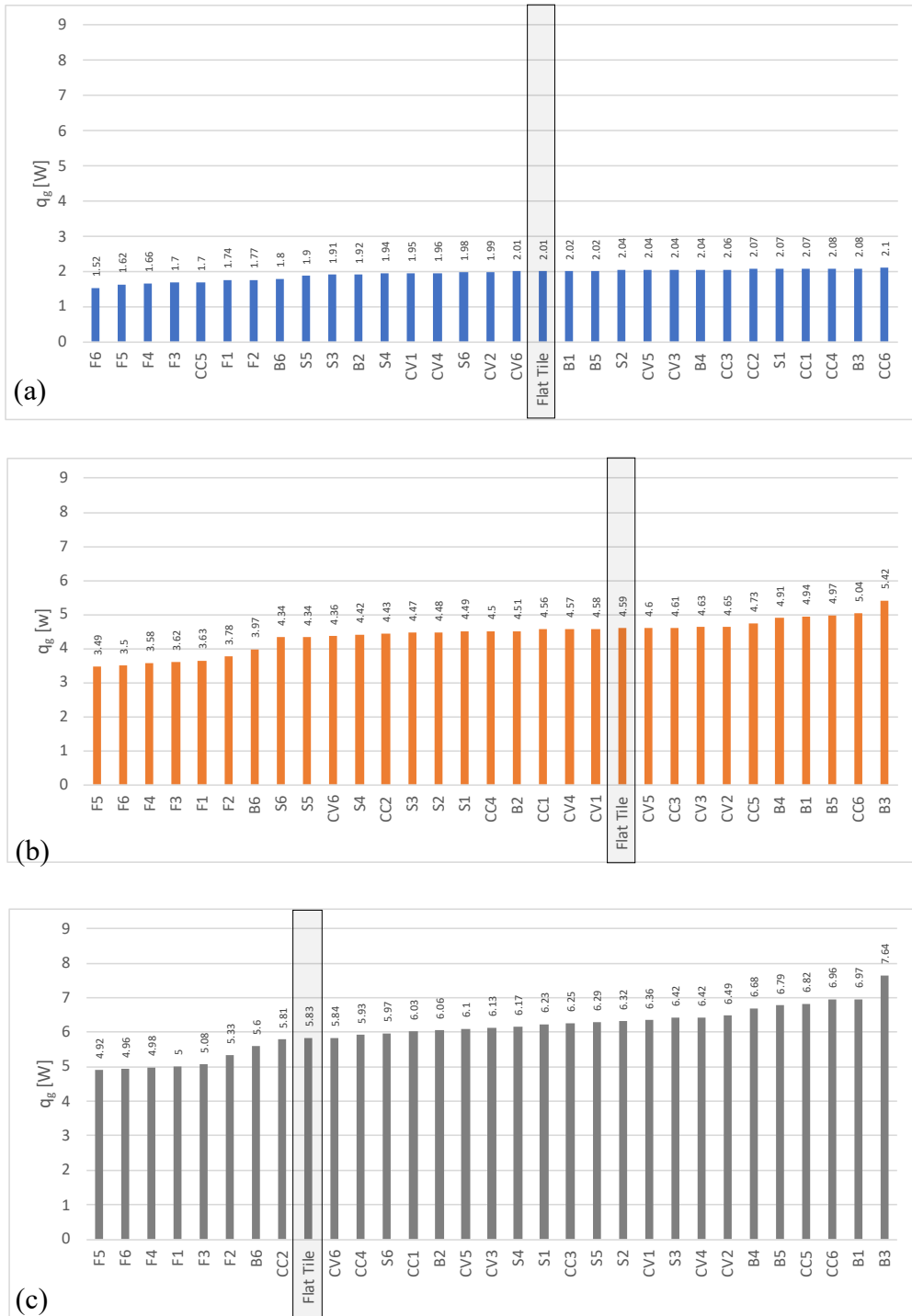


**Fig. 9.** Global heat transfer rates for  $U_j =$  (a) 1 m/s, (b) 5 m/s, (c) 10 m/s.

	1 m/s		5 m/s		10 m/s	
B1	-0.50%		-7.63%		-19.55%	
B2	4.48%		1.74%		-3.95%	
B3	-3.48%		-18.08%		-31.05%	
B4	-1.49%		-6.97%		-14.58%	
B5	-0.50%		-8.28%		-16.47%	
B6	10.45%		13.51%		3.95%	
CC1	-2.99%		0.65%		-3.43%	
CC2	-2.99%		3.49%		0.34%	
CC3	-2.49%		-0.44%		-7.20%	
CC4	-3.48%		1.96%		-1.72%	
CC5	15.42%		-3.05%		-16.98%	
CC6	-4.48%		-9.80%		-19.38%	
CC7	0.50%		-3.49%		-9.95%	
CV1	2.99%		0.22%		-9.09%	
CV2	1.00%		-1.31%		-11.32%	
CV3	-1.49%		-0.87%		-5.15%	
CV4	2.49%		0.44%		-10.12%	
CV5	-1.49%		-0.22%		-4.63%	
CV6	0.00%		5.01%		-0.17%	
CV7	-1.99%		0.22%		-5.32%	
Flat Tile	0.00%		0.00%		0.00%	
F1	13.43%		20.92%		14.24%	
F2	11.94%		17.65%		8.58%	
F3	15.42%		21.13%		12.86%	
F4	17.41%		22.00%		14.58%	
F5	19.40%		23.97%		15.61%	
F6	24.38%		23.75%		14.92%	
F7	20.40%		23.53%		14.92%	
F8	23.88%		24.84%		16.47%	
S1	-2.99%		2.18%		-6.86%	
S2	-1.49%		2.40%		-8.40%	
S3	4.98%		2.61%		-10.12%	
S4	3.48%		3.70%		-5.83%	
S5	5.47%		5.45%		-7.89%	
S6	1.49%		5.45%		-2.40%	

**Fig. 10.** Improvement factors [Eq. (1)] of investigated tiles.  
Red = degradation; blue = enhancement of insulating performance.

Fig. 10 presents the improvement factor for all investigated tiles and velocities. The most significant improvement was observed within the Fur group, whereby all investigated velocities achieved lower heat transfer rates when compared to smooth tiles. The minimum and maximum improvement factors in this group were  $I = 8.58\%$  (F2 at  $U_j = 10$  m/s) and  $I = 24.84\%$  (F8 at  $U_j = 5$  m/s) respectively. Another tile that

showed improvement compared to the result of the smooth tile, at all investigated velocities, was B6 ( $3.95\% < I < 10.45\%$ ). While no other group indicated consistent improvement for all geometries and velocities, the following tiles mostly showed improvement with relatively low degradation: CV6 ( $-0.17\% < I < 5.01\%$ ) and CC2 ( $-2.99\% < I < 3.49\%$ ).

### **3.1 Inspiration from Nature: Geometry Improvement**

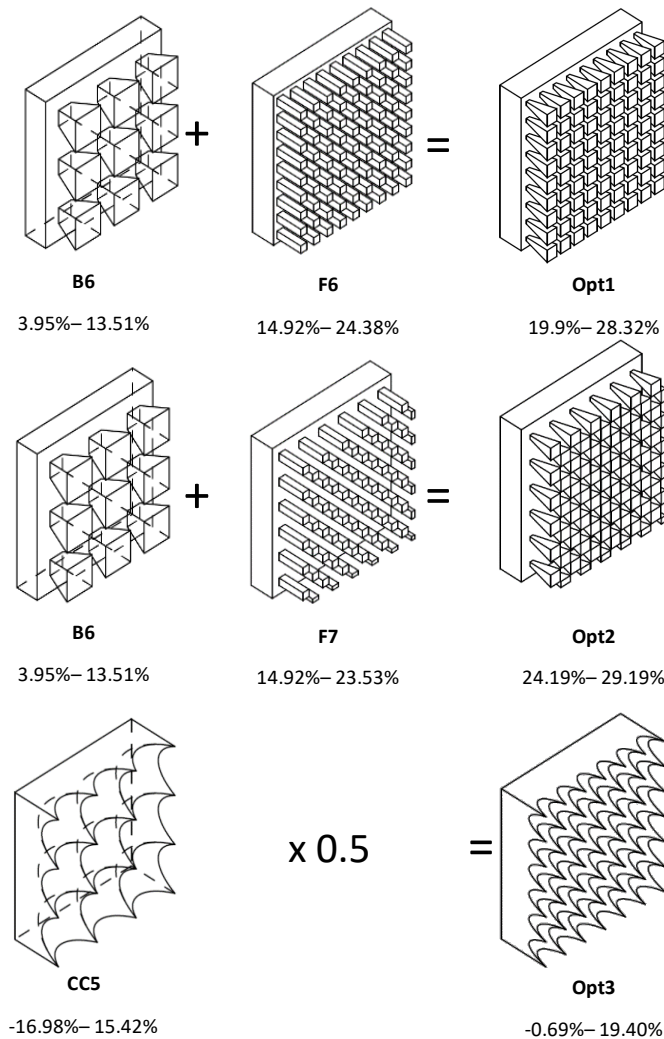
Based on the knowledge of the tiles that achieved the best results (as indicated in Fig. 9), potential geometrical characteristics could be identified for creating new hybrid geometries that outperform our initial designs. This was first done by combining high-performing tiles from different groups into optimized (Opt) configurations as shown in Fig. 11: (i) B6 and F6 (linear arrangement, “Opt1”); and (ii) B6 and F7 (diagonal arrangement, “Opt2”).

As expected, these new synergetic, optimized geometries achieved improved results. The first geometry (Opt1) increased the improvement factor from  $I = 19.9\%$  (at 1 m/s) to 28.32% (at 5 m/s), while the second geometry (Opt2) increased  $I$  from 24.19% (at 10 m/s) to 29.19% (at 5 m/s).

Looking at these two improved designs, one notices that the density of the geometric elements significantly increased. Therefore, densifying a geometry was further explored. For example, the repetitive geometric element in CC5 was scaled down by half, multiplying the number of elements per unit area accordingly (Fig. 11, bottom row, “Opt3”). The new tile significantly improved thermal insulating performance compared to the previous design (CC5), with improvement factors increasing from  $I = 15.42\%$  to 19.4% at 1 m/s; from  $I = -3.05\%$  to 15.25% at 5 m/s;

and from  $I = -16.98\%$  to  $-0.69\%$  at 10 m/s.

**Fig. 11.** Geometry improvements and associated ranges (in percentages) of  $I$ .



### 3.2 Tile Surface Area Versus Global Heat Transfer Rate

The examined tiles were defined by several properties, including dimensions (width, length, and height), shape, volume, weight, and surface area. Some of these dimensions were kept identical intentionally (width and length, for example), while others were changed in order to alter the geometry (exposed surface area, for example). By significantly altering this area, some geometric tiles had an exposed surface area that was between 1.3 and almost 5 times larger than the smooth tile (as shown in Table 1). Since the geometries created for this research were "carved" into

the flat tile, their exposed surface area was larger while their volume was smaller than that of the smooth tile. In this section, the relation between the exposed surface area and the resulting global heat transfer rates were examined, while in the next section the effect of tile volume will be discussed.

For every geometry, the surface area ratio (SAR) was determined as the ratio between the exposed surface area of the examined tile and that of the smooth baseline tile. Bodies with a larger SAR tend to transfer more heat than those with a smaller one (Bergman et al., 2007). For instance, homes lose more heat through larger windows than through smaller ones, considering they have the same glass composition and thickness. Additionally, a larger roof loses more heat than a smaller one, considering they have the same insulation characteristics. That is why radiators are often designed to have a large surface area, in order to improve heat transfer.

In contrast to common building-design practices where the SAR is minimized, our results plotted in Fig. 12 imply that increasing the SAR could lead to improved insulating performance of the specific geometries. For every wind speed investigated, the higher the SAR, the lower the  $q_g$  (Fig. 12), and the sculptured tile provides better insulation (Fig. 12). Moreover, the least-square linear fits (dotted lines in Fig. 12) indicate that the effect increases with increasing  $U_j$  (decreasing slopes of the fits).

As air is known to serve as an insulator – a barrier that limits heat transfer – this could provide an explanation for the reduced global heat transfer that we found in our research. The tiles with the sculptured surfaces had the enhanced capability of entrapping air inside their cavities, thereby increasing their insulating properties. Evidence for this conjecture can be seen in the contour plot that is depicted in Fig. 13. This illustration presents the magnitude of the velocity vectors that were obtained from the CFD simulation, for tiles with trapezoidal cavities (CV6). It can clearly be observed that the velocity within the cavities is close to zero. Moreover, it should be noted that at a velocity of 5 m/s, the improvement factor was  $I = 5.01\%$  for this case (as seen in Fig. 10).

The Fur group is noticeably the best at entrapping air, which is not surprising considering that fur is used to keep animals warm, creating insulating layers by

entrapping air. Even at relatively low SAR values (about 2.0, Fig. 12), The Fur tiles achieved the best results. Interestingly, the Fur group's performance was not sensitive to SAR and remained approximately the same for  $SAR > 2.0$ .

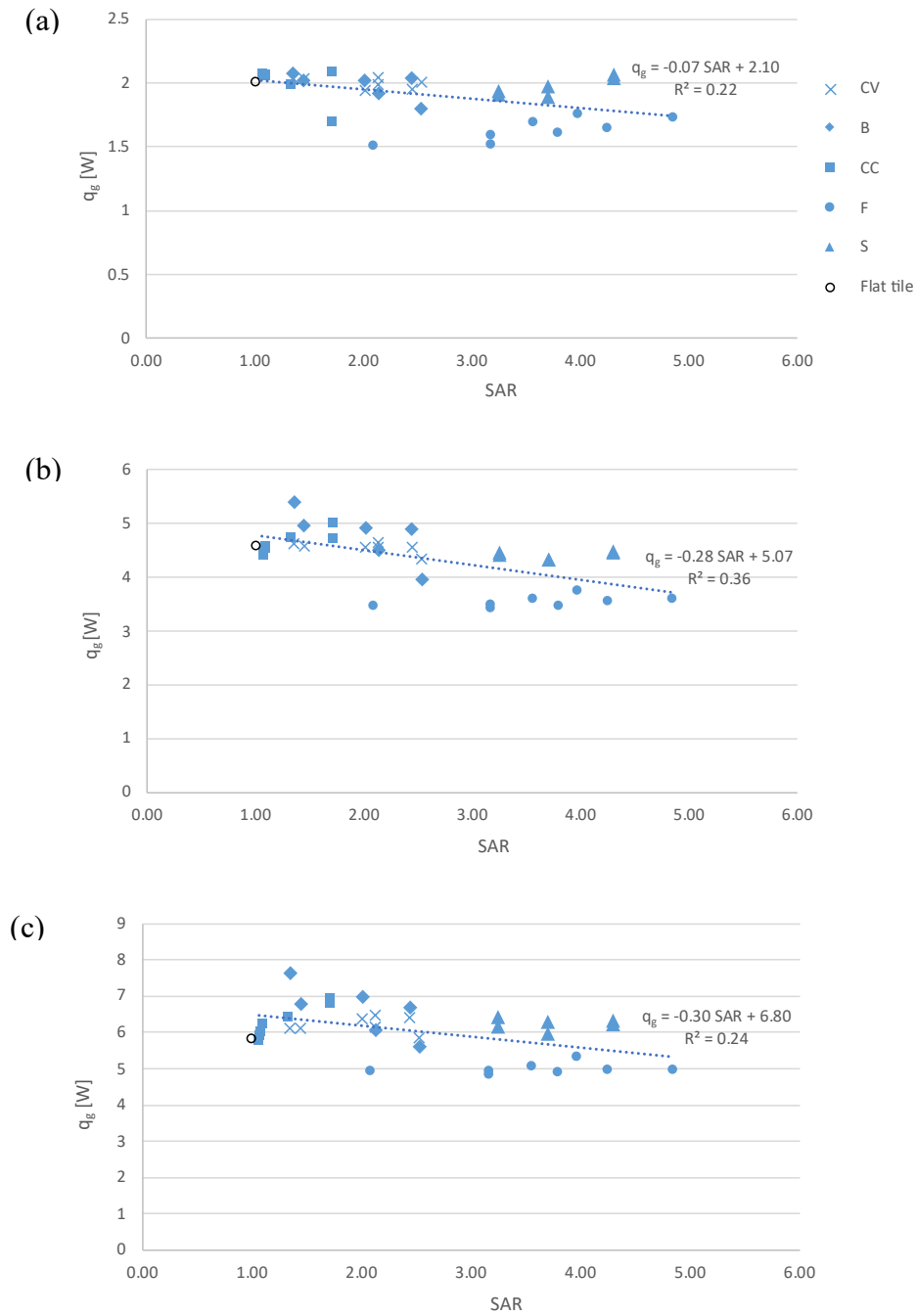


**Fig. 12.** Global heat transfer rates versus SAR for different geometric tiles.  $U_j =$  (a) 1 m/s; (b) 5 m/s; (c) 10 m/s.

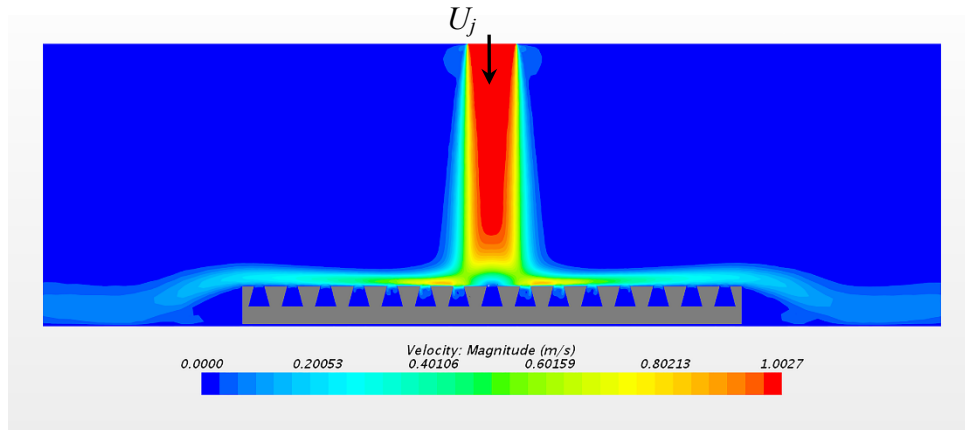


**Fig. 13.** Contour plots of the velocity magnitude in plane crossing the jet's centerline for the jet impinging on CV6 at a wind speed of 5 m/s. RANS simulation, Star-CCM+.

### 3.3 Tile volume versus global heat transfer rate

When conducting the research, we investigated whether insulation performance can be maintained while significantly saving on building materials at the same time. For every examined geometry, the volume ratio, VR, was defined as the ratio between the volume of the examined tile and that of the smooth baseline one. The values of the different tiles ranged from VR = 0.43 (F1) to VR = 0.95 (CV3), as shown in Table 1. Tiles with global heat transfer rates that were within +/- 0.1W of the baseline value are presented in Fig. 14 together with their VR values. Our results revealed that these tiles saved about 10% to 38% on material compared to the flat tile, while providing the same thermal performance. Note that similar results were found for wind speeds of 5 and 10 m/s.



**Fig. 14.** Volume ratio of tile geometries having global heat transfer rates similar to those of the baseline flat tile (within +/- 0.1 W) at 1 m/s. Results are arranged by decreasing VR.

### 3.4 Effect of Solar Irradiance

Up to this stage radiation was not taken into account. The radiation results of several tiles are compared to those of the baseline tile in Fig. 15 that shows the monthly average solar irradiance for tiles that were located on a south facing façade. In general, for all geometries, the graphs show lower solar irradiance values during the summer months and higher ones during the winter. This is common for south facing façades due to the sun's changing angles between summer and winter (Lechner, 2014). In the Cavities group, the average solar irradiance increased during the winter months by 4.5% (CV6) to 14.5% (CV5), while in the summer months it increased by 4.2% (CV6) to 11.6% (CV5). Our results showed that the Cavities group had a positive effect during the wintertime, as they contributed to passive heating. However, they did not improve passive cooling during the summer.

The results for the Cacti group, however, were diverse. The CC1 and CC2 tiles increased the average solar irradiance in both winter (from 7.5% to 25%) and summer (from 12.5% to 21%), while CC3 tiles decreased it in both seasons (on average 15% and 17% in winter and summer, respectively). Of the examined tiles, CC3 was the only one that contributed to passive cooling during the summer months, yet it did not improve passive heating in winter. In conclusion, for the majority of the investigated tiles, the self-shading phenomenon does not seem to reduce the radiative heat load on

the building façade. Further research is needed to examine and optimize the performance of the geometries that did show such a reduction.

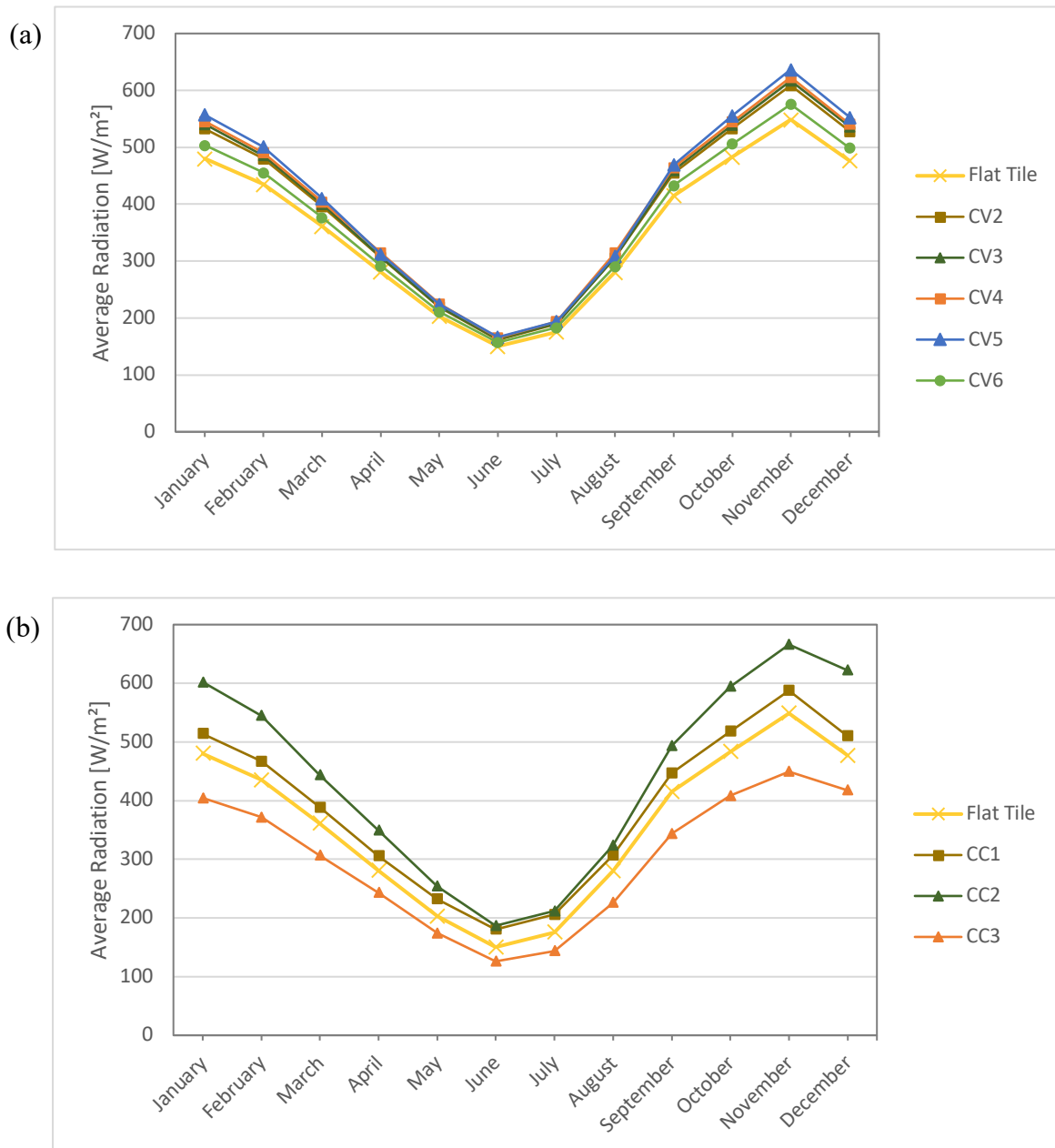


**Fig. 15.** Monthly Averaged Solar Irradiance [ $\text{W}/\text{m}^2$ ]

### 3.5 The Overall Heat Transfer Coefficient

To compare the performance of the developed, sculptured tiles to that of standard

building materials, the overall heat transfer coefficient,  $U$ , of the tiles is required. The schematic cross-section of a sculptured tile is depicted in Fig. 16. It should be noted that subscripts “i” and “o” denote inner and outer wall respectively. The global heat transfer rate (not taking *radiation* into account) between the inner wall and the free stream temperature,  $T_{\infty,o}$ , is calculated as follows (Bergman et al., 2007):

$$q_g = \frac{T_{\infty,o} - T_i}{\left[ \frac{\Delta x}{kA_i} + \frac{1}{h_o A_o} \right]} \quad (2)$$

In this equation,  $h_o$  denotes the convective heat transfer coefficient at the outside wall;  $\Delta x$  is the wall thickness; and  $k$  its thermal conductivity. Only for a flat tile, the inner wall surface area,  $A_i$ , equals that of the outer wall,  $A_i = A_o$ . This equation can also be written in terms of the overall heat transfer coefficient based on the inner wall surface:

$$q_g = U_i A_i (T_{\infty,o} - T_i) \quad (3)$$

For this equation,  $(T_{\infty,o} - T_i) = 7^\circ\text{C}$ , and  $U_i$  is given by:

$$U_i = \frac{1}{\left[ \frac{\Delta x}{k} + \frac{A_i}{h_o A_o} \right]} \quad (4)$$

For the investigated tiles, the values of  $U_i$  were determined according to equation 4 and are presented in Table 2.

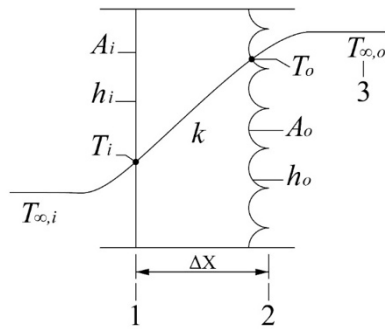


**Fig. 16.** Schematic cross-section of a geometric tile including parameters used in equation 4.

As mentioned earlier, the examined tiles were scaled down to one-fifth of their original size (1:5 scale) to suit the experimental set-up, while the same tile size was numerically simulated to ensure consistency. In order to estimate the overall heat

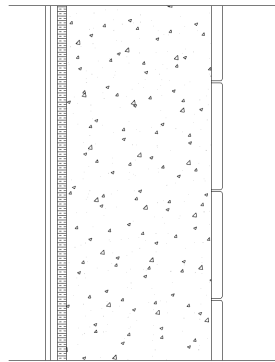
transfer coefficients of real-size tiles, the changing thickness and surface area must be considered. Looking at Equation 3, contributions to  $U_i$  stem from both convection and conduction. An estimate of the actual overall heat transfer coefficient can be obtained using the following simplification: Assuming that the convective heat transfer coefficient ( $h_o$ ) and the  $A_i/A_o$  ratio remain constant, the only resistance that changes is the one that is related to conduction ( $\Delta x/k$ ) and that governs the expression for  $U_i$  in Equation 4. Note that for simplicity in the scaling argument, we assume 1D heat conduction although the actual conduction is three-dimensional (as taken into account in the numerical simulations). Therefore, increasing the thickness of the tile by a factor of five will increase the resistance associated with conduction by about the same factor, and  $U_i$  of an actual tile will become about five times smaller than that of the simulated tile. The obtained overall heat transfer coefficients from the simulations were scaled in this manner and are given in Table 2.

$U_j$	1 m/s	5 m/s	10 m/s
B1	1.44	3.53	4.98
B2	1.37	3.22	4.33
B3	1.49	3.87	5.46
B4	1.46	3.51	4.77
B5	1.44	3.55	4.85
B6	1.29	2.84	4.00
CC1	1.48	3.26	4.31
CC2	1.48	3.16	4.15
CC3	1.47	3.29	4.46
CC4	1.49	3.21	4.24
CC5	1.21	3.38	4.87
CC6	1.50	3.60	4.97
CC7	1.43	3.39	4.58
CV1	1.39	3.27	4.54
CV2	1.42	3.32	4.64
CV3	1.46	3.31	4.38
CV4	1.40	3.26	4.59
CV5	1.46	3.29	4.36
CV6	1.44	3.11	4.17
CV7	1.46	3.27	4.39
Flat Tile	1.44	3.28	4.16
F1	1.24	2.59	3.57
F2	1.26	2.70	3.81
F3	1.21	2.59	3.63
F4	1.19	2.56	3.56
F5	1.16	2.49	3.51
F6	1.09	2.50	3.54
F7	1.14	2.51	3.54
F8	1.09	2.46	3.48
S1	1.48	3.21	4.45
S2	1.46	3.20	4.51
S3	1.36	3.19	4.59
S4	1.39	3.16	4.41
S5	1.36	3.10	4.49
S6	1.41	3.10	4.26

**Table 2.** Overall heat transfer coefficients ( $U$ -values, Eq. (4)) of real-size tiles for all measured wind velocities. Note: Units =  $[W/m^2K]$ ; size of real tiles = (100cm×100cm×7.5cm).

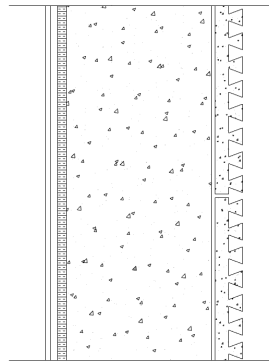
These  $U$ -values enable the estimation of a tile's effect on the thermal performance of a wall. Fig. 17(a) shows a cross-section of an exterior concrete wall with typical interior and exterior finishes. In addition to layer thicknesses ( $d$ ) and their thermal conductivities ( $k$ ), layer thermal resistances ( $r = d/k$ ) can also be calculated. The resistance associated with convective heat transfer at the interior side of the wall was estimated to be  $r_i = 0.13 \text{ m}^2\text{K}/\text{W}$ , while that associated with convective heat transfer at the exterior wall ( $r_o$ ) was included in the  $U$ -value that was obtained by the simulations.

(a) Typical concrete wall detail (stone cladding)



Layers	Thickness (cm)	r (m <sup>2</sup> K/W)
Stone	2.2	0.04
Concrete	40	0.75
Mineral Wool	2.5	0.50
Gypsum	1.3	0.01
<b>r<sub>i</sub> = 0.13 (m<sup>2</sup>K/W)</b>		
<b>R = 1.44 (m<sup>2</sup>K/W)</b>		
<b>U (1 / R) = 0.69 (W/m<sup>2</sup>K)</b>		

(b) Concrete wall detail, type CV6



Layers	Thickness (cm)	r (m <sup>2</sup> K/W)
Concrete tile: CV6	7.5	0.69
Concrete	40	0.75
Mineral Wool	2.5	0.50
Gypsum	1.3	0.01
<b>r<sub>i</sub> = 0.13 (m<sup>2</sup>K/W)</b>		
<b>R = 2.09 (m<sup>2</sup>K/W)</b>		
<b>U (1 / R) = 0.48 (W/m<sup>2</sup>K)</b>		

**Fig. 17.** Wall details and thermal data. All layers in (b) are similar to those in (a) except for the stone cladding.

Summation of the thermal resistances of the different layers results in the total thermal resistance of the wall (i.e.,  $R = r_1 + r_2 + r_3 \dots$ ). This is used to calculate the U-value of the composite wall:  $U = 1/R$  [W/m<sup>2</sup>K]. For evaluating the wall performance, one of the tested tiles (CV6) was chosen, with a thickness of 7.5cm and thermal resistance of 0.69 m<sup>2</sup>K/W (CFD simulation at 1 m/s, as shown in Table 2). A new wall combination was developed, replacing the stone cladding with the CV6 concrete tiles. Calculations of the overall heat transfer coefficient indicated that the tiles improved thermal resistance by 33%, as seen in Fig. 17(b).

#### 4. Discussion and Conclusions

Rigid conventions dominate the field of building insulation, with today's insulation

methods hardly differing from those that were used a century ago. These usually entail a high thermal mass combined with layers of insulating materials. This research introduces a novel direction into the architectural discourse, suggesting the use of geometric manipulations as a means for improving thermal insulation, and promoting a new way of thinking in relation to building envelopes.

This paper presented the development of a cladding, sculptured tiles bank, organized into groups, where tiles in each group have similar geometric characteristics but different scaling. The characteristics and principles of these geometries can be utilized when creating new complex designs. For example, the guiding principles of density, shape, and size may be implemented in parametric designs, to create changing geometries that adjust their performance according to airflow and climatic conditions. In addition, aesthetical complex geometries for building envelopes could be developed based on those same guiding principles. The paper presented a methodology for the development of sculptured tiles that combined both CFD experiments and simulations, leveraging the high reliability of the former and the efficiency of the latter.

About half of the tested cases showed an improvement in their thermal performance compared to smooth tiles, with performance depending on the wind speed. The most significant improvements were seen in the geometries mimicking animal fur that achieved heat transfer rates up to 24.84% lower than those achieved by the smooth tiles. By combining the geometrical characteristics of the best performing tiles, we created a hybrid geometry that achieved an even higher improvement factor of 29.19%. Moreover, we found that tiles with higher SAR achieved better thermal insulation (i.e., exhibited lower global heat transfer rates), and tiles with global heat transfer rates that were similar to those of the baseline value saved about 10% to 38% on materials compared to the flat tiles. Finally, when examining radiation heat transfer, we found that the self-shading phenomenon did not reduce the radiative heat load on the building façade.

The possible wall combinations discussed in Section 3 (see also Fig. 17) indicate

that the developed “nature-inspired” tile could significantly contribute to the building industry in a number of directions. While it may not be able to serve as a substitute for the traditional approach to thermal insulation in buildings, it does have the potential to significantly improve building insulation, especially in renovation projects of ill-insulated buildings.

**Acknowledgements:** This work was supported by the Israeli Ministry of Construction and Housing [grant number 2022402/2015].

## 5. References

- Badarnah, L., & Knaack, U. (2008). Organizational features in leaves for application in shading systems for building envelopes. *Design and Nature IV: Comparing Design in Nature with Science and Engineering*, 87–96. WIT Press.
- Badarnah, L., Nachman Farchi, Y., & Knaack, U. (2010). Solutions from nature for building envelope thermoregulation. *Comparing design and nature with science and engineering*, 251-262.  
[https://uwe-repository.worktribe.com/preview/982008/Badarnah\\_DesignNature2010.pdf](https://uwe-repository.worktribe.com/preview/982008/Badarnah_DesignNature2010.pdf)
- Behnia, M., Parneix, S., & Durbin, P. A. (1998). Prediction of heat transfer in an axisymmetric turbulent jet impinging on a flat plate. *International Journal of Heat and Mass Transfer*, 41(12), 1845-55.  
[https://doi.org/10.1016/S0017-9310\(97\)00254-8](https://doi.org/10.1016/S0017-9310(97)00254-8)
- Bergman, T. L., Incropera, F. P., DeWitt, D. P., & Lavine, A. S. (2011). *Fundamentals of heat and mass transfer*. John Wiley & Sons.
- Cupkova, D., & Azel, N. (2015). Mass regimes: Geometric actuation of thermal behavior. *International Journal of Architectural Computing*, 13(2), 169-93.  
<https://doi.org/10.1260/1478-0771.13.2.169>
- Fecheyr-Lippens, D., & Bhiwapurkar, P. (2017). Applying biomimicry to design building envelopes that lower energy consumption in a hot-humid climate. *Architectural Science Review*, 60(5), 360-70.  
<https://doi.org/10.1080/00038628.2017.1359145>
- Golany, G. S. (1996). Urban design morphology and thermal performance. *Atmospheric Environment*, 30(3), 455-65.  
[https://doi.org/10.1016/1352-2310\(95\)00266-9](https://doi.org/10.1016/1352-2310(95)00266-9)
- Golneshan, A. A., & Yaghoubi, M. A. (1990). Simulation of ventilation strategies of a residential building in hot arid regions of Iran. *Energy and Buildings*, 14(3), 201-205.  
[https://doi.org/10.1016/0378-7788\(90\)90043-I](https://doi.org/10.1016/0378-7788(90)90043-I)

- Grobman, Y. J. (2008). Building the digital world – Architectural design methods based on the use of digital tools – Performance based form generation and optimization. [Doctoral dissertation, Technion – Israel Institute of Technology]. [https://grobman.net.technion.ac.il/files/2013/03/final\\_phd\\_thesis-92008-web.pdf](https://grobman.net.technion.ac.il/files/2013/03/final_phd_thesis-92008-web.pdf)
- Grobman, J., Taragan, H., & Gal, N. (2010). Soft [ware] boundaries: complex geometry in architectural design. The beauty of Japheth in the tents of Shem: studies in honor of Mordechai Omer. Tel Aviv: Tel Aviv University, 585-599.
- Grobman, Y. J. (2013, January 7-9). Cellular building envelopes. *International Conference on Research Into Design (ICoRD)*, Madras, Chennai. <https://grobman.net.technion.ac.il/files/2013/01/cellular-building-envelopes.pdf>
- Grobman, Y. J., & Neuman, E. (Eds.). (2013). *Performatism: form and performance in digital architecture*. Routledge.
- Grobman, Y. J., & Elimelech, Y. (2015). Microclimate on building envelopes: Testing geometry manipulations as an approach for increasing building envelopes' thermal performance. *Architectural Science Review*, 59(4), 269-78. <https://doi.org/10.1080/00038628.2015.1025688>.
- Hauer, E. (2004). *Continuous architectural walls and screens*. Princeton Architectural Press.
- Hershovich, C., van Hout, R., Rinsky, V., Laufer, M., & Grobman, J. Y. (2017, May). Microclimate on building envelopes: Wind tunnel and computational fluid dynamic analysis of basic and complex geometries. *The Symposium on Simulation for Architecture and Urban Design (SimAUD)*. Toronto, Canada.
- Hrynuik, J. T., Van Luipen, J., & Bohl, D. (2012). Flow visualization of a vortex ring interaction with porous surfaces. *Physics of Fluids*, 24(3). <https://doi.org/10.1063/1.3695377>
- Latifi Khorasgani, M., Prohasky, D., Burry, J., Moya Castro, R., McCarthy, J. & Watkins, S. (2016). Breathing skins for wind modulation through morphology: toward integrating turbulence studies within tectonic scale for design of façade components. *Proceedings of the 21st International Conference of the Association*

*for Computer-Aided Architectural Design Research in Asia.*

[https://www.researchgate.net/profile/Jesse\\_Mccarthy/publication/299821428\\_BREATHING\\_SKINS\\_FOR\\_WIND\\_MODULATION\\_THROUGH\\_MORPHOLOGY/links/5705c67808aef745f717704d.pdf](https://www.researchgate.net/profile/Jesse_Mccarthy/publication/299821428_BREATHING_SKINS_FOR_WIND_MODULATION_THROUGH_MORPHOLOGY/links/5705c67808aef745f717704d.pdf)

Laver, J., Clifford, D., & Vollen, J. (2008). High performance masonry wall systems: Principles derived from natural analogues. *Design and Nature IV: Comparing Design in Nature with Science and Engineering*, 243–52. WIT Press.

Lechner, N. (2014). Heating, cooling, lighting: Sustainable design methods for architects. John Wiley & Sons.

Montazeri, H., & Blocken, B. (2013). CFD simulation of wind-induced pressure coefficients on buildings with and without balconies: Validation and sensitivity analysis. *Building and Environment* 60, 137-49.  
<https://doi.org/10.1016/j.buildenv.2012.11.012>

Seibold, Z., Hinz, K., García del Castillo y López, J. L., Alonso, N. M., Mhatre, S., & Bechthold, M. (2018). Ceramic morphologies: Precision and control in paste-based additive manufacturing. In *ACADIA // 2018: Recalibration. On Imprecision and Infidelity. [Proceedings of the 38th Annual Conference of the Association for Computer Aided Design in Architecture (ACADIA) ISBN 978-0-692-17729-7] Mexico City, Mexico 18-20 October, 2018, Pp. 350-357. CUMINCAD.*  
[http://papers.cumincad.org/data/works/att/acadia18\\_350.pdf](http://papers.cumincad.org/data/works/att/acadia18_350.pdf).

Stanford, A. (2004). *Eladio Dieste—Innovation in Structural Art*. Princeton Architectural Press.

Van Hout, R., Rinsky, V., Grobman, Y., 2018a. Experimental study of a round jet impinging on a flat surface: flow field and vortex characteristics in the wall jet. *Int. J. of Heat and Fluid Flow* 70, 41-58. doi:10.1016/j.ijheatfluidflow.2018.01.010

Van Hout, R., Rinsky, V., Hershovich, C, Grobman, Y., 2018b. Outer layer characteristics of a radially expanding wall jet on smooth and dimpled surfaces. *Int. J. of Heat and Fluid Flow*, 72, 304-316.

<https://doi.org/10.1016/j.ijheatfluidflow.2018.06.011>

Van Hout, R., Rinsky, V., Sasson, N., Hershovich, C, Tshuva, M., Grobman, Y.,  
2018c. Axisymmetric jet impingement on a dimpled surface: Effect of  
impingement location on flow field characteristics. *Int. J. of Heat and Fluid Flow*,  
74, 53-64. <https://doi.org/10.1016/j.ijheatfluidflow.2018.09.010>

Waters, J. K. (2003). *Blobitecture: Waveform architecture and digital design*.  
Rockport Publishers.

Zuckerman, N., & Lior, N. (2005). Impingement heat transfer: Correlations and  
numerical modeling. *Journal of Heat Transfer*, 127(5), 544-52  
<https://doi.org/10.1115/1.1861921>